JACS
JOURNAL OF THE AMERICAN CHEMICAL SOCIETY
Article
pubs.acs.org/JACS

Structure of the Reduced Copper Active Site in Preprocessed Galactose Oxidase: Ligand Tuning for One-Electron O_2 Activation in Cofactor Biogenesis

Ryan E. Cowley,[†] Jordi Cirera,[†,⊥] Munzarin F. Qayyum,[†] Dalia Rokhsana,[‡,#] Britt Hedman,[†,§] Keith O. Hodgson,[†,§] David M. Dooley,*[,‡,∥] and Edward I. Solomon*[,†,§]

[†]Department of Chemistry, Stanford University, Stanford, California 94305, United States
[‡]Department of Chemistry and Biochemistry, Montana State University, Bozeman, Montana 59717, United States
[§]Stanford Synchrotron Radiation Lightsource, SLAC National Accelerator Laboratory, Stanford University, Menlo Park, California 94025, United States
[∥]University of Rhode Island, Kingston, Rhode Island 02881, United States

Supporting Information

ABSTRACT: Galactose oxidase (GO) is a copper-dependent enzyme that accomplishes $2e^-$ substrate oxidation by pairing a single copper with an unusual cysteinylated tyrosine (Cys-Tyr) redox cofactor. Previous studies have demonstrated that the post-translational biogenesis of Cys-Tyr is copper- and O_2-dependent, resulting in a self-processing enzyme system. To investigate the mechanism of cofactor biogenesis in GO, the active-site structure of Cu(I)-loaded GO was determined using X-ray absorption near edge structure (XANES) and extended X-ray absorption fine structure (EXAFS) spectroscopy, and density-functional theory (DFT) calculations were performed on this model. Our results show that the active-site tyrosine lowers the Cu potential to enable the thermodynamically unfavorable $1e^-$ reduction of O_2, and the resulting Cu(II)$-O_2^{\bullet-}$ is activated toward H atom abstraction from cysteine. The final step of biogenesis is a concerted reaction involving coordinated Tyr ring deprotonation where Cu(II) coordination enables formation of the Cys-Tyr cross-link. These spectroscopic and computational results highlight the role of the Cu(I) in enabling O_2 activation by $1e^-$ and the role of the resulting Cu(II) in enabling substrate activation for biogenesis.

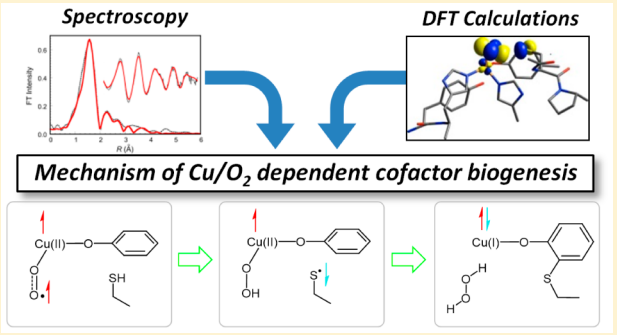

1. INTRODUCTION

Galactose oxidase (GO) is a secretory fungal enzyme that catalyzes the $2e^-$ oxidation of primary alcohols to aldehydes (Scheme 1A)[1−5] and some evidence suggests GO may also capable of the subsequent slower $2e^-$ oxidation to carboxylic acids (Scheme 1B).[6,7] Each of these reactions is coupled to the $2e^-$ reduction of O_2 to H_2O_2. The native substrate of GO is D-galactose;[8] however, a broad range of other sugar and aromatic alcohol substrates are also active, which has led to the proposal that the physiological role of GO is the generation of H_2O_2, perhaps as a defense against pathogenic organisms.[9] GO is also an important component in electrochemical biosensors of galactose that are used for various biotechnology applications.[10−12] Despite accomplishing $2e^-$ reduction of O_2, the active site of GO contains only a single Cu. To provide the additional redox equivalent required for turnover, the active-site Cu is coordinated by a unique cysteinylated tyrosine (Cys-Tyr) ligand that serves as a second redox-active cofactor.[13,14] The low (Cys-Tyr)$^\bullet$ reduction potential (0.45 V) relative to unmodified Tyr$^\bullet$ (0.95 V) indicates that the role of cysteinylation (as well as π-stacking of an adjacent conserved Trp)[15] is to stabilize (Cys-Tyr)$^\bullet$ and allow its function as a redox cofactor at a more biologically accessible potential. Therefore, in turnover, the Cu/(Cys-Tyr) unit accomplishes $2e^-$ redox by shuttling between Cu^I/(Cys-Tyr)$^-$ and Cu^{II}/(Cys-Tyr)$^\bullet$ states in a ping-pong type mechanism (Scheme 1C).[1]

To form mature active GO, the expressed preprocessed protein[16] undergoes a series of post-translational modifications to remove leader peptides, and, most importantly, cross-link cysteine with tyrosine to form the Cys-Tyr cofactor. This oxidative cofactor biogenesis reaction is also catalyzed by Cu bound to the active site, and has been reported to occur aerobically with either the Cu(I) or Cu(II) form,[17] or anaerobically with Cu(II).[18] The aerobic Cu(I)-dependent biogenesis reaction is significantly faster than with Cu(II) (by a factor of ~10^4), suggesting that it is the biologically relevant

Received: June 6, 2016
Published: September 14, 2016

ACS Publications © 2016 American Chemical Society

DOI: 10.1021/jacs.6b05792
J. Am. Chem. Soc. 2016, 138, 13219−13229

Scheme 1

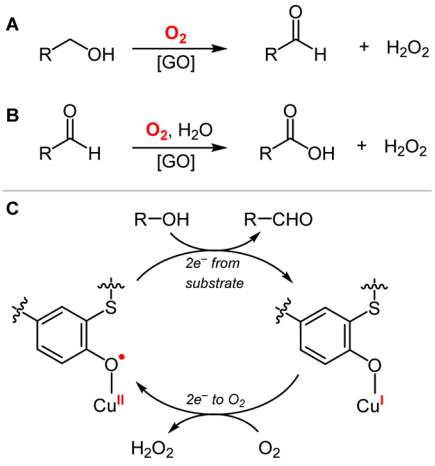

biogenesis reaction in vivo;[17] however, Cu(II)-dependent biogenesis might also be relevant in the anaerobic trans-Golgi network.[18] The focus of this study is to understand the mechanism of aerobic Cu(I) biogenesis, which is particularly interesting because the reduction potential associated with the aqueous $1e^-$ reduction of O_2 to $O_2^{\bullet-}$ is uphill (−0.16 V)[19] while that of the $2e^-$ reduction of O_2 to H_2O_2 is downhill (+0.28 V)[19] and therefore favored, as in the functional reaction with both Cu and Tyr-Cys cofactors present. Thus, it is important to understand the thermodynamic factors that enable the $1e^-$ activation of O_2 by a single Cu center.

The crystal structure of the processed (cofactor formed) Cu(II) site reveals the active site ligation (PDB 1GOF, Figure 1).[14] Residues His496, His581, cysteinylated-Tyr272, and an

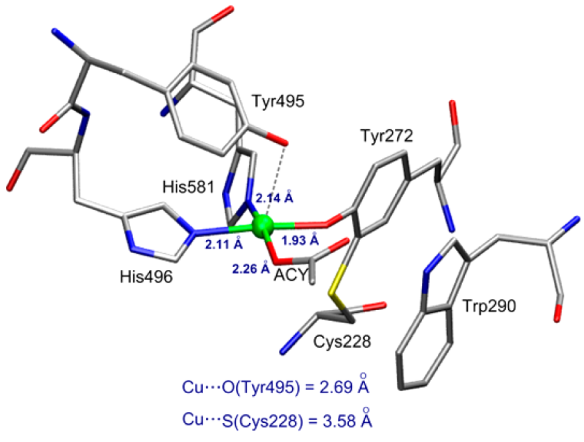

Figure 1. Active site structure of processed Cu(II)-GO (PDB 1GOF).[14] The equatorial acetate ligand (ACY) is not present when crystallized in the absence of acetate, leaving an open position for substrate coordination.[20]

acetate (ACY) ion form the four equatorial ligands. In the structure of Cu(II)-GO crystallized without acetate (PDB 1GOG),[14] the fourth equatorial position is occupied by a weakly bound water ($Cu-OH_2$ = 2.8 Å). A second tyrosine (Tyr495) occupies an axial position with a Cu−O 2.6−2.7 Å distance in these structures. Since no crystal structure exists of Cu(I) GO (neither the preprocessed nor mature form), we have spectroscopically characterized the geometric structure of the preprocessed Cu(I) active site using Cu K-edge X-ray absorption spectroscopy (XAS). The structural results of the experimental data are correlated to density functional theory (DFT) calculations, which are used to understand the unique properties of the site that enable $1e^-$ O_2 activation and to determine the mechanism of cofactor biogenesis.

2. MATERIALS AND METHODS

2.1. XAS Sample Preparation. Apo preprocessed GO was expressed and purified as previously described.[18] An aliquot of apo preprocessed GO was taken from a stock solution (50 mM PIPES, pH 6.8) and buffer exchanged into 50 mM phosphate (pH 6.5). The solution was degassed in a crimp-top vial under N_2 for 30 min and transferred to a glovebox under N_2 atmosphere. The GO protein solution was concentrated to ∼0.5 mM using a centrifuge filter, and 0.8 equiv of Cu(I) (as a 20 mM solution of $[Cu(NCMe)_4]PF_6$ in acetonitrile) was added, followed by 20 wt % sucrose. This preprocessed Cu(I)-GO sample was loaded into 2 mm thick Lucite XAS cells wrapped with a translucent layer of 38 μm Cu-free Kapton tape, which formed the cell windows. The filled sample cells were immediately frozen and stored under liquid N_2. The amount of Cu(II) in the samples was quantified to be <1% by EPR.

2.2. XAS Data Acquisition. The Cu K-edge XAS data were measured at the Stanford Synchrotron Radiation Lightsource (SSRL) on the focused 16-pole, 2.0 T wiggler beamline 9−3. Storage ring parameters were 3 GeV and 80−100 or 500 mA. A Rh-coated premonochromator mirror was used for harmonic rejection and vertical collimation, while a cylindrical, bent Rh-coated postmonochromator mirror was used for focusing. A Si(220) double-crystal monochromator was used for energy selection. The samples were maintained at a constant temperature of ∼10 K during data collection using an Oxford Instruments CF 1208 continuous-flow liquid helium cryostat. A Canberra solid-state Ge 30- or 100-element array detector was used to collect Kα fluorescence with a Zn filter aligned at 90° to the outgoing fluorescence signal. The sample was positioned 45° to the incident beam. Internal energy calibration was accomplished by simultaneous measurement of the absorption of a Cu foil placed between two ionization chambers located after the sample. The first inflection point of the foil spectrum was assigned to 8980.3 eV.

EXAFS data are reported to k = 12.8 $Å^{-1}$ in order to avoid interference from the Zn K-edge. No photodamage was observed, and thus all scans were used in the final signal average. Four data sets of samples prepared from different batches of protein were collected, and each data set included an average of 22 scans. All four sets of EXAFS data were fit separately and provided equivalent metrical parameters.

2.3. XAS Data Analysis. The energy-calibrated and averaged data were processed by fitting a second-order polynomial to the pre-edge region and subtracting this from the entire spectrum as a background. A three-region polynomial spline of orders 2, 3, and 3 was used to model the smoothly decaying postedge region. The data were normalized by scaling the spline function to an edge jump of 1.0 at 9000 eV. This background subtraction and normalization was done using PySpline.[21] The least-squares fitting program OPT in EXAFSPAK[22] was used to fit the data. Initial ab initio theoretical phase and amplitude functions were generated in FEFF 7.0[23] using the DFT-optimized structure of Cu(I)-GO described in subsection 2.4 as the starting model. Atomic coordinates were adjusted as necessary as fits were improved. During the fitting process, the bond distance (R) and the mean-square deviation or bond variance in R arising from thermal and static disorder (σ^2) were varied for all components. The threshold energy (E_0), the point at which the photoelectron wave vector k = 0 was also allowed to vary for each fit but was constrained to the same value for all components in a given fit. Coordination numbers (N) were systematically varied to provide the best chemically viable agreement to the EXAFS data and their FT but were fixed within a given fit. The fits were evaluated based on comparison of the normalized error (F_n) of each fit along with inspection of individual wave components.

2.4. Molecular Modeling of the Preprocessed Cu(I)-GO Active Site and Biogenesis Reaction Coordinate. Density

DOI: 10.1021/jacs.6b05792
J. Am. Chem. Soc. 2016, 138, 13219−13229

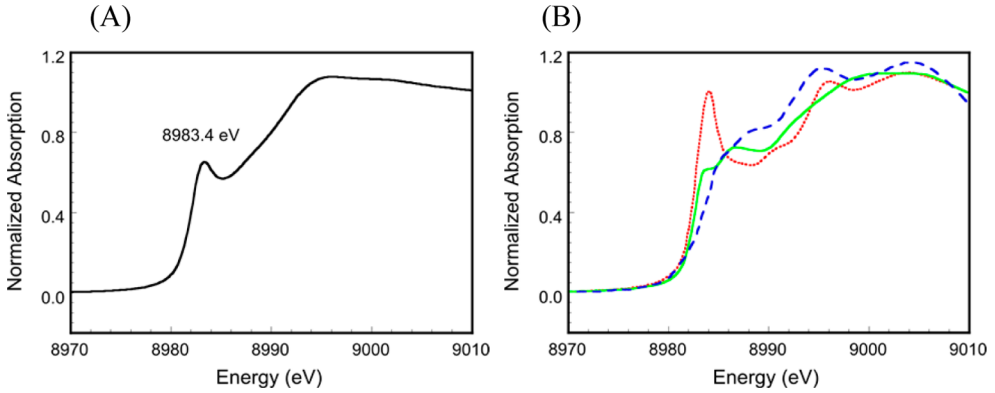

Figure 2. Normalized Cu K-edge XAS spectrum of (A) preprocessed Cu(I)-GO and (B) model complexes with two-coordinate Cu(I) (red dots, $[Cu_2(EDTB)]^{2+}$), three-coordinate Cu(I) (green line, $[Cu_2(mxyN_6)]^{2+}$), and four-coordinate Cu(I) (blue dashes, $[Cu(tepa)]^{+}$).[26] EDTB = *N*,*N*,*N*′,*N*′-tetrakis(2′-benzimidazolylmethyl)-1,2-ethanediamine;[27] $mxyN_6$ = 1,3-bis(bis[2-(3,5-dimethyl-1-pyrazolyl)ethyl]amino)benzene;[28] tepa = tris(2-[2-pyridyl]ethyl)amine.[29]

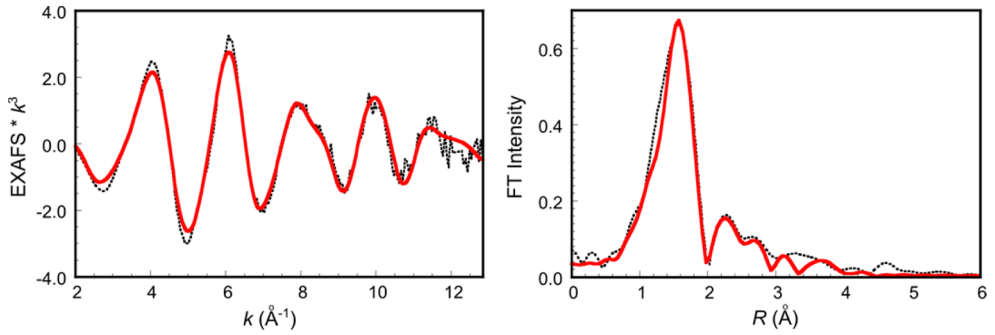

Figure 3. Cu K-edge EXAFS data (A) and nonphase-shift-corrected Fourier transform (B) of preprocessed Cu(I)-GO. The phase shift in the first shell is ∼0.4 Å. The data are shown in black, and Fit A is shown in red. Fits B and C are shown in Figures S1 and S2.

functional theory (DFT) calculations were carried out with Gaussian 09 (A.01 and C.01)[24] using a 10^{-8} convergence criterion in the density matrix. A triple-ζ all-electron Gaussian basis set was employed for all the elements, adding polarization functions for the Cu, O, N, and C centers. A hybrid BP86 functional with 38% of Hartree−Fock exchange, previously optimized for mononuclear copper sites was used in all calculations.[25] Parallel calculations including Grimme's D3 dispersion correction (Figure S3) or using the B3LYP functional (with 20% HF exchange, Figure S4) gave qualitatively similar results. A polarized-continuum model was used with $\varepsilon = 4$ in all calculations to account for solvation in the protein medium.

Geometry optimized structures of the preprocessed Cu(I)-GO active site were obtained starting from the modified crystallographic parameters of apo preprocessed GO (2VZ1)[16] as well as from processed Cu(II)-GO (1GOF),[14] yielding similar results. For all optimizations, the positions of the β carbons in all residues were fixed in order to preserve the overall shape of the active site. The structure derived from 1GOF was used to bind dioxygen to obtain the end-on bound Cu(II)-superoxo species optimized for the triplet ($S = 1$) ground state. The triplet wave function was then used to generate the optimized structure of the broken symmetry ($M_s = 0$) solution. For the virtual mutation studies, the coordinated Tyr272 was manually replaced with histidine, fluoride, or hydroxide to obtain three optimized structures, and their end-on Cu(II)-superoxo structures were obtained as described above for the triplet ($S = 1$) and broken symmetry ($M_s = 0$) spin states.

3. RESULTS

3.1. X-ray Absorption Spectroscopy. *3.1.1. XANES.* The Cu K-edge X-ray absorption near edge structure (XANES) of Cu(I) species provides a probe of the coordination number, since the intense 1s → 4p electric dipole-allowed ($\Delta l = \pm 1$) transition exhibits spectral shapes characteristic of 2-, 3-, and 4-coordinate Cu(I) sites (Figure 2B). From correlation to model data, the intensity and energy position (8983.4 eV) of the 1s → 4p transition in the Cu K-edge XANES of preprocessed Cu(I)-GO (Figure 2A) is characteristic of a 3-coordinate Cu(I) species.[26]

3.1.2. EXAFS. The extended X-ray absorption fine structure (EXAFS) region carries quantitative structural and ligation information on the absorbing atom. The EXAFS and its nonphase shifted Fourier transform (FT) of preprocessed Cu(I)-GO is shown in Figure 3. The best fit parameters (Fit A) are given in Table 1. The first shell is fit with a 3-coordinate Cu−N/O vector at an average distance of 2.01 ± 0.03 Å with a reasonable bond variance (σ^2) of 0.00710 Å^2 (Fit A).[30] Split first-shell fits were also attempted with 1 short Cu−O/N and 2

Table 1. EXAFS Least-Squares Fitting Results (Fit A) for Preprocessed Cu(I)-GO Using the Data Range k = 2-12.8 Å^{-1}

coord. no./path	R (Å)[a]	σ^2 (Å^2)[b]	ΔE_0 (eV)	F_n[c]
3 Cu−O/N	2.01	710	−10.83	0.056
5 Cu−C	2.93	758		
10 Cu−N/O−C	3.03	312		
4 Cu−N−C	4.30	942		

[a]The estimated standard deviation in R for each fit is ±0.02 Å. [b]The σ^2 values are multiplied by 10^5. [c]The normalized error, F_n, is given by $\Sigma[(\chi_{obsd} - \chi_{calcd})^2 k^6]/N_{data}$. The error in coordination number is 25%, and that in the identity of the scatterer Z is ±1.

DOI: 10.1021/jacs.6b05792
J. Am. Chem. Soc. 2016, 138, 13219−13229

long Cu−N/O (Fit B, Figure S1) and 2 short Cu−O/N and 1 long Cu−N/O (Fit C, Figure S2) vectors, with fit parameters given in Table S1. The differences in the split first-shell distances of Fits B and C are 0.14 and 0.13 Å, respectively, which are near the resolvable difference in the distances from EXAFS data collected to k of 12.8 Å^{-1} (0.14 Å resolution). Fit B is a reasonable alternative to Fit A, however a 2-component fit to the first shell is not justified based on the limited data range. In addition, the σ^2 value for the 2Cu−O/N path of Fit C is large (0.00714 Å^2) compared to that of the higher coordination number 3Cu−O/N path in Fit A. Fits with a Cu−S vector at distances of 2.1−2.8 Å^{-1} were not unique and yielded high σ^2 values of 0.02000 Å^2 and thus were not reasonable, indicating Cys228 does not coordinate to preprocessed Cu(I)-GO. The second shell of the FT between R of 2.4−2.8 Å was fit with 5 Cu−C single-scatterers (from 2His and 1Tyr) and the corresponding 10 Cu−N/O-C and 4 Cu−N−C multiple-scattering paths to give the final EXAFS Fit A (Table 1, Figure 3).

The EXAFS data thus reveal that the Cu(I) in GO is coordinated to three N or O donor atoms at an average distance of 2.01 ± 0.03 Å, although the data range limits the ability to split the distances. Since there are two His and two Tyr residues that could coordinate to the Cu(I), there are two possible combinations of donor atoms (2His/1Tyr or 1His/2Tyr) that are consistent with the XANES/EXAFS results. Since metal−ligand bonds get progressively shorter with higher metal oxidation state, a useful tool to distinguish N from O ligation is bond valence sum (BVS) analysis, which uses a library of compounds of known structure and oxidation state to estimate the contributions of each ligand bond to the observed oxidation state in an unknown complex.[31−33] BVS analysis has been used in EXAFS analysis in a variety of Cu metalloproteins to correlate structure with oxidation state.[34−37] The bond valence sum (V) is the charge on the metal ion that is calculated using eq 1, where r_i is the observed metal−ligand bond length from EXAFS, and r_0 and B are empirically determined parameters.[38]

$$V = \sum_i e^{(r_0 - r_i/B)} \quad (1)$$

The BVS results are summarized in Table 2. A coordination of 1O/2N for Cu(I) preprocessed GO predicts V = 0.99, which closely reproduces the Cu(I) oxidation state observed in XANES, while a 2O/1N coordination sphere slightly underestimates the charge (V = 0.93). This suggests a 1O/2N formulation with 2 His (His496 and His581) and 1 Tyr (Tyr 272) coordinated to the copper center is more consistent with the EXAFS data than a 2O/1N formulation. The experimental bond lengths are also consistent with available crystallographic data for Cu(I) complexes.[39]

Table 2. Calculated BVS Values for 2N/1O and 2O/1N Coordination to Cu at 2.01 Å

2His + 1Tyr				1His + 2Tyr			
ligand	r_i	r_0	$\frac{r_0 - r_i}{B}$	ligand	r_i	r_0	$\frac{r_0 - r_i}{B}$
O	2.01	1.550	0.29	O	2.01	1.550	0.29
N	2.01	1.662	0.35	O	2.01	1.550	0.29
N	2.01	1.662	0.35	N	2.01	1.662	0.35
		V = 0.99				V = 0.93	

3.2. Cu(I) Active Site Modeling.

Two in silico models were used to perform optimizations to obtain the preprocessed Cu(I)-GO active site. One model used the crystal structure of apo preprocessed GO (2VZ1)[16] with Cu(I) manually added as the starting structure, while the other used the crystal structure of processed Cu(II)-GO (1GOF)[14] with the Cys-Tyr cross-link manually removed. In both cases, the model included Cys228, Tyr272, Tyr495, His496, and His581 residues. Tyr 495 and His 581 were truncated at the β carbons (i.e., modeled as methyl groups), while the backbone connecting Tyr495 and His496 was kept intact and Cys228 included the full amino acid and the first two atoms of Phe227 for added flexibility. Both 2VZ1- and 1GOF-derived models were optimized and yielded very similar structures with virtually identical geometries and metal−ligand bond lengths (Table 3). The optimized structure shows a T-shaped, three-coordinate Cu(I) with 2 short bonds to the *trans* Tyr272 (Cu−O = 1.95 Å) and His496 (Cu−N = 1.97 Å), and one longer bond to His581 (Cu−N = 2.14 Å) (Figure 4). The coordination sphere at Cu(I) is nearly planar, with Cu lying 0.3 Å out of the 2His/Tyr plane. The average Cu−N/O bond length in the optimized model (2.02 Å) is in agreement with the EXAFS data (Table 1, 2.01 Å), and the simulated

Table 3. Structural Parameters (Å; deg) for the Optimized Active Site of Preprocessed Cu(I)-GO Modeled from 1GOF and 2VZ1 Crystal Structures

	1GOF	2VZ1
Cu−O(Tyr272)	1.946	1.940
Cu−N(His496)	1.966	1.966
Cu−N(His581)	2.139	2.155
Cu−L(average)	2.017	2.020
∠N−Cu−N	100.4	97.3
∠N(His496)−Cu−O	150.9	149.2
∠N(His581)−Cu−O	99.5	104.2
∠N−N−Cu−O[a]	21.3	22.2

[a]Pyramidalization; defined as the deviation of Cu out of the 2His1Tyr trigonal ligand field.

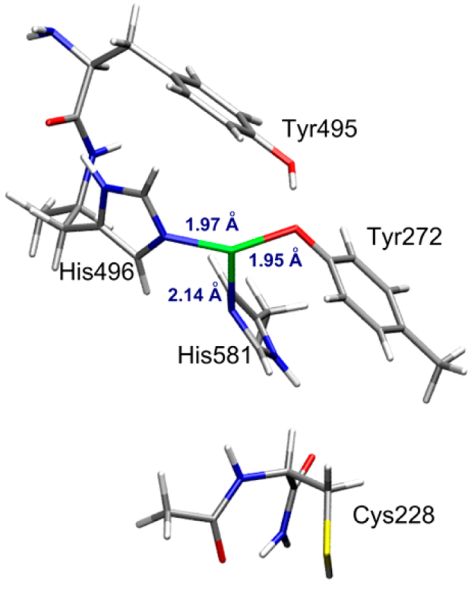

Figure 4. DFT optimized structure of preprocessed Cu(I)-GO modeled from the 1GOF crystal structure.

DOI: 10.1021/jacs.6b05792
J. Am. Chem. Soc. 2016, 138, 13219−13229

EXAFS of this model reasonably reproduces the experimental data (Figure S6). Other isomers of preprocessed Cu(I)-GO were evaluated computationally, however all were at least 5 kcal/mol higher in energy than the 2His1Tyr structure.[40]

3.3. O_2 Activation by the Cu(I) Active Site. *3.3.1. Geometric and Electronic Structure.* The DFT-optimized structure of the Cu(I) preprocessed active site (Figure 4) was used to evaluate its reactivity toward dioxygen. Dioxygen binds to mononuclear copper centers in models of metalloenzyme active sites, forming either side-on[41−44] (η^2) or end-on[45−58] (η^1) species, which lead to different electronic structures. Active site optimizations were performed with O_2 bound to the copper center in both η^1 and η^2 configurations and in both triplet and singlet spin states. Regardless of the starting configuration, both optimizations led to an end-on (η^1) O_2-bound structure (Figure 5); a stable η^2-O_2 configuration could not be located. In the

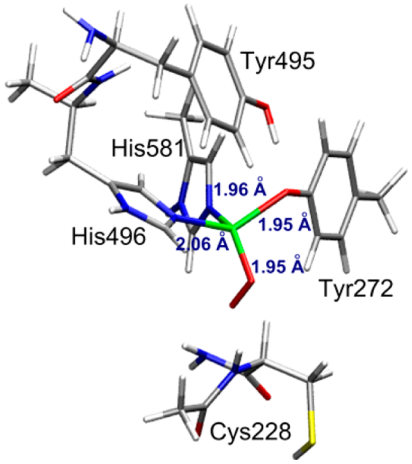

Figure 5. DFT-optimized structure of end-on coordination of superoxide to preprocessed Cu(I)-GO.

optimized η^1-O_2 structure, the O−O bond length (1.292 Å, cf. free O_2 at 1.21 Å) is indicative of a one-electron reduction of O_2 to the superoxo level, and is consistent with the 1.280 Å O−O bond observed by crystallography in a $Cu^{II}(O_2^{\bullet-})$ model complex.[49] The Cu center displays a D_{2d}-distorted tetrahedral geometry (Table 4) with a terminal superoxide ligand.

The end-on O_2-bound species has two holes: one localized in the Cu $d_{x^2-y^2}$ orbital, and the second in the O_2 π^* antibonding orbital, indicating that an electron has transferred from Cu(I) to dioxygen forming a Cu(II)-superoxo species. This species can have two different electronic configurations: a triplet (S = 1) ground state, where the unpaired electrons on Cu and O_2 have the same spin (Table 4), or a singlet (S = 0) ground state, where the two spins are antiferromagnetically coupled. For the singlet solution, broken symmetry (BS) wave functions (M_s = 0) were generated. Formation of $^3[Cu^{II}(O_2^{\bullet-})]$ from $^3O_2$ and Cu^I-GO is approximately thermoneutral (ΔG° = +1.3 kcal/mol at 298 K), while $^1[Cu^{II}(O_2^{\bullet-})]$ is higher in energy by 5.3 kcal/mol (spin-corrected $\Delta G^\circ_{S=0}$ = +6.6 kcal/mol). Thus, the ground state of the end-on Cu(II)-superoxo is S = 1, consistent with the experimentally determined triplet ground state in all end-on cupric superoxo model complexes.[45,46]

3.3.2. Activation of the Cu(I) Site in Preprocessed GO. Since the one-electron reduction of O_2 is uphill (E° = −160 mV for the $O_{2(aq)}/O_2^{\bullet-}{}_{(aq)}$ couple),[19] Cu(I) must be reducing enough, and/or the Cu(II)−($O_2^{\bullet-}$) bond strong enough, to

Table 4. Structural Parameters, Charges, and Spin Densities of the Optimized O_2−Bound Active Site of Preprocessed Cu(I)-GO

bond or angle		value
Cu−O_2		1.954 Å
O−O		1.292 Å
Cu−O(Tyr272)		1.950 Å
Cu−N(His496)		2.060 Å
Cu−N(His581)		1.961 Å
∠Cu−$O_{proximal}$−O_{distal}		82.6°
∠N(His496)−Cu−O(Tyr272)		131.1°
∠N(His581)−Cu−$O_{proximal}$		147.3°
atom or group	natural charge[a]	Mulliken spin
Cu	+1.46	+0.62
$O_{proximal}$	−0.27	+0.63
O_{distal}	−0.32	+0.59
Tyr272	−0.42	−0.01
His496	−0.12	+0.10
His581	−0.44	0.00

[a]Charges calculated from Natural Bond Orbital analysis.

compensate in order to result in an overall thermoneutral reaction. Tyr272 was selectively varied in silico to His, F^-, and OH^- in order to evaluate the role of this equatorial ligand in O_2 binding and reduction. For each computational variant, the analogous end-on $^3[Cu^{II}(O_2^{\bullet-})]$ was >5 kcal/mol more stable than the corresponding $^1[Cu^{II}(O_2^{\bullet-})]$, as in WT GO (Table 5). The free energies of O_2 binding to the Tyr272(F^-) (ΔG = +2.1 kcal/mol) and Tyr272(OH^-) (ΔG = +3.9 kcal/mol) models were calculated to be similar to that in WT (+1.3 kcal/mol). However, the Tyr272His computational model showed significantly less favorable O_2 binding free energy (ΔG = +9.7 kcal/mol) than any of the variants with an anionic equatorial ligand. This is primarily due to a less favorable O_2 binding enthalpy (ΔH = −2.5 kcal/mol in Tyr272His versus −10.2 kcal/mol in WT), while the entropic difference in O_2 binding is similar between Tyr272His and WT ($T\Delta S$= −12.3 kcal/mol and −11.5 kcal/mol, respectively). The O_2 binding for all of the computational variants was further decomposed into two contributions (Figure 6): (1) the reduction potential of the active site (ΔG_1 in Table 5), calculated from the outer-sphere 1e^- electron transfer from Cu(I) to O_2 and including PCM solvation correction; and (2) the strength of the Cu(II)-$O_2^{\bullet-}$ bond formed (ΔG_2 in Table 5), calculated from the binding energy of $O_2^{\bullet-}$ to the Cu(II) site.

From the energy diagram in Figure 6, the dominant contribution to O_2 binding in preprocessed Cu(I)-GO comes from the decreased reduction potential (ΔG_1, Table 5) due to the anionic equatorial ligand providing ∼0.6−1.0 eV (13−24 kcal/mol) additional driving force relative to a neutral histidine ligand. $O_2^{\bullet-}$ coordination to Cu(II) (ΔG_2, Table 5) is very favorable for all variants. Binding of superoxide to Cu(II) has a similar entropic cost (9 ± 3 kcal/mol) for all variants, however the bonding interaction between the negatively charged superoxide and Cu(II) is destabilized by 12−20 kcal/mol (ΔH_2, Table 5) when Cu is coordinated by an anionic ligand relative to the neutral His ligand. The destabilizing effect of the negative charge of the equatorial ligand on the Cu−O_2 bond strength is thus compensated (and for Tyr^-, outweighed) by the additional driving force supplied by the lower reduction potential.

DOI: 10.1021/jacs.6b05792
J. Am. Chem. Soc. 2016, 138, 13219−13229

Table 5. Thermodynamics of O_2 Binding to Cu(I) (kcal/mol at 298 K) in Preprocessed WT GO and in Silico Tyr272X (X = His, OH^-, F^-) Variants

		overall O_2 binding			outer-sphere ET		$O_2^{\bullet-}$ binding		
variant	$Cu^{II}(O_2^{\bullet-})$ spin state	ΔH	$T\Delta S$	ΔG	ΔG_1	ΔE_1[a]	ΔH_2	$T\Delta S_2$	ΔG_2
WT	$S = 1$	−10.2	−11.5	+1.3	+41.8	–	−51.3	−10.8	−40.5
	$S = 0$	−6.9	−13.5	+6.6					
Tyr272His	$S = 1$	−2.5	−12.3	+9.7	+60.6	+0.82	−63.0	−12.1	−50.9
	$S = 0$	+3.4	−7.8	+11.2					
Tyr272(OH^-)	$S = 1$	−8.1	−10.2	+2.1	+36.7	−0.22	−43.0	−8.4	−34.6
Tyr272(F^-)	$S = 1$	−5.6	−9.5	+3.9	+47.7	+0.26	−49.7	−5.9	−43.8

[a]Calculated change in $Cu^{2+/1+}$ potential (V) relative to WT.

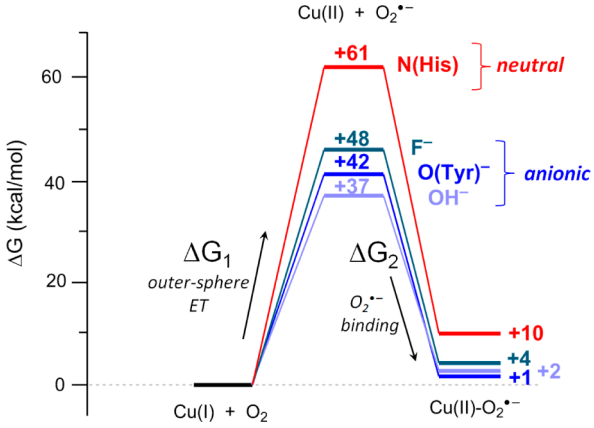

Figure 6. Calculated thermodynamics of O_2 binding to WT Cu(I)-GO and in silico Tyr272X (X = His, OH^-, F^-) variants, shown as the sum of outer-sphere electron transfer (ΔG_1) and $O_2^{\bullet-}$ binding (ΔG_2) energies. All energies are given in free energy (kcal/mol) at 298 K.

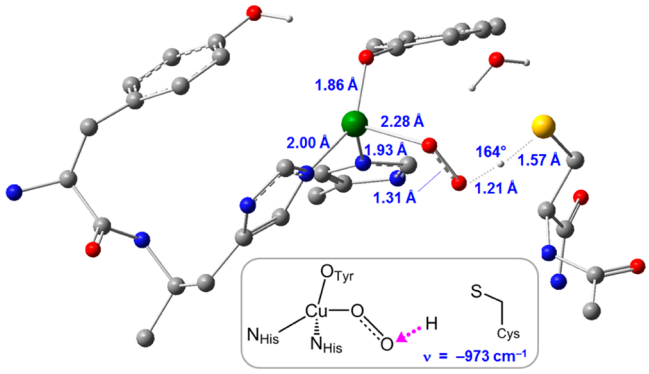

Figure 7. DFT-optimized structure of H atom abstraction from Cys228 by $^3[Cu^{II}(O_2^{\bullet-})]$ in preprocessed GO. Inset: Imaginary frequency corresponding to H atom transfer (magenta arrow).

Thus, the calculations show that the reactivity of dioxygen with the preprocessed Cu(I)-GO active site to form the end-on superoxo Cu(II) triplet species is largely driven by the favorable effect of the negatively charged Tyr ligand on the Cu(I) potential. Even though the free energy associated with the outer sphere $1e^-$ redox process to form Cu(II)-GO and superoxo fragments is unfavorable, the strong Cu(II)-superoxo binding interaction provides sufficient driving force to make the overall process approximately thermoneutral in WT GO (ΔG = +1.3 kcal/mol).

3.4. Cofactor Biogenesis. *3.4.1. H-Atom Abstraction.* Due to their reactive O_2 π^* frontier molecular orbitals, Cu(II) superoxo complexes are activated toward H atom abstraction (HAA).[50,51,59−61] In preprocessed GO, an end-on cupric superoxo species would likely uptake one of the accessible H atoms in the vicinity of the active site. From the available candidates within ∼5 Å (Tyr495, Tyr272, and Cys228), the only thermodynamically accessible hydrogen atom is the S−H on Cys228, in which H atom abstraction by $Cu^{II}(O_2^{\bullet-})$ to yield Cu^{II}−OOH and Cys-S$^\bullet$ is calculated to be modestly endergonic (ΔG = +9.2 kcal/mol for the H atom abstraction step; ΔG = +10.4 kcal/mol from Cu(I) + O_2 reactants). HAA from Tyr272 (*ortho* C−H), Tyr495 (O−H) or the Cys228 backbone (N−H) are all highly unfavorable (ΔG = +40.8, + 21.8, and +41.2 kcal/mol, respectively, see Table S1). HAA from Cys228 proceeds with a barrier of $\Delta G^{\ddagger}$ = +16.1 kcal/mol (+17.4 kcal/mol from Cu(I) + O_2 reactants) on the triplet surface, with the transition state shown in Figure 7. The product of HAA is Cu(II)-OOH, with the radical originating from $O_2^{\bullet-}$ now transferred to cysteine as Cys-S$^\bullet$, positioned ∼6 Å away from Cu(II). Mulliken spin analysis shows 0.12 e^- of spin density has been transferred to the sulfur at the transition state, and 0.97 e^- in the Cys-S$^\bullet$ product. Without a superexchange pathway, the two spins (on Cu(II) and Cys-S$^\bullet$) are not coupled, and thus both spin states (S = 1 and S = 0) are isoenergetic. This spatial uncoupling of the α and β spins allows facile crossover from the triplet to the singlet spin surface at this stage of the reaction (which is required for the cross-link, vide infra).

3.4.2. Cys-Tyr Cross-linking. The final step for cofactor biogenesis requires the attack of Cys-S$^\bullet$ on the ortho carbon of Tyr272. The attack of Cys-S$^\bullet$ to give a dearomatized ring with sp^3 hybridization at the ortho carbon (with the proton remaining on the ring) was calculated to have a high barrier ($\Delta G^{\ddagger}$ = 32.3 kcal/mol, see Figure 8), which is too large to be consistent with the reaction kinetics from experiment (k = 0.4 s^{-1} at pH 7,[17] which gives $\Delta G^{\ddagger} \approx$ 18 kcal/mol). However, deprotonation of the cross-linked Cys-Tyr product would have a very large driving force (ΔG = −44.2 kcal/mol), which suggests that the large barrier for cross-linking originates from the unfavorable dearomatization of the Tyr ring. The driving force for ring deprotonation could potentially be used to lower the cross-link barrier if deprotonation occurs with C−S cross-linking in a concerted step. This was investigated by calculating a two-dimensional potential energy surface (Figure 9A) in which the radical sulfur atom of Cys228 approaches the ortho carbon of Tyr272 while the ortho hydrogen of Tyr272 is deprotonated by a nearby water molecule. This water molecule is included to bridge the Cu^{II}−OOH and Tyr272 and serves as a proton shuttle in a Grotthuss-type mechanism[62,63] to transfer the H^+ to the proximal O of the hydroperoxide.[64] From the saddle point of the surface in Figure 9A, the energy barrier for the concerted cross-link/deprotonation process is ∼14 kcal/mol (i.e., a total barrier of ∼20 kcal/mol from Cu(I) + O_2

DOI: 10.1021/jacs.6b05792
J. Am. Chem. Soc. 2016, 138, 13219−13229

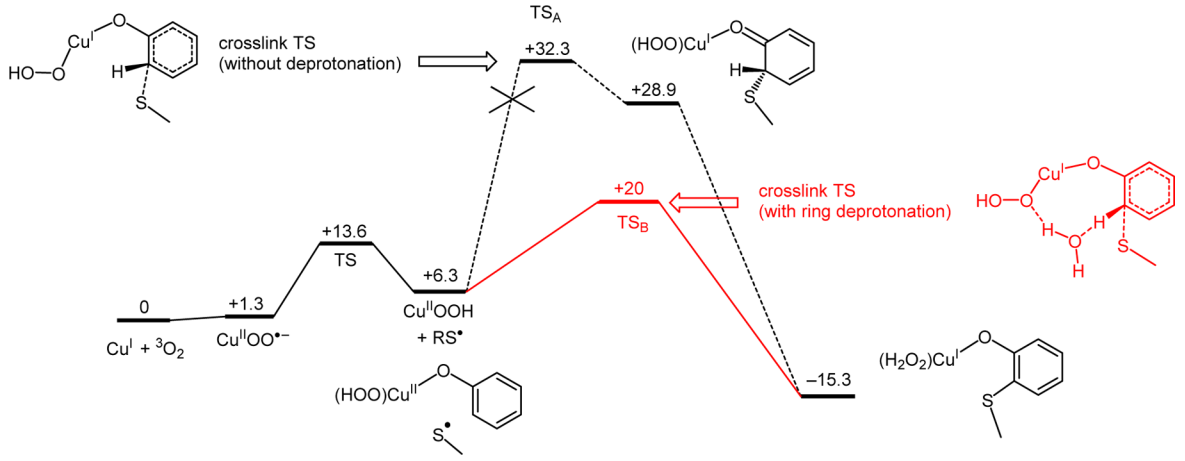

Figure 8. Cu(I)-dependent cofactor biogenesis reaction coordinate, with free energies (ΔG and $\Delta G^{‡}$) in kcal/mol at 298 K.

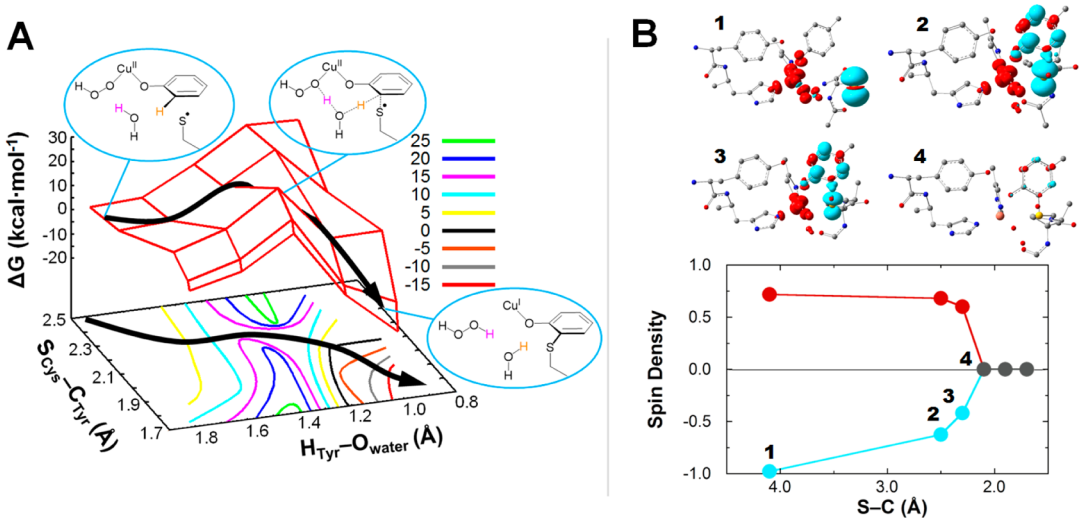

Figure 9. (A) Two-dimensional potential energy surface of Cys-Tyr cross-link formation concerted with ring deprotonation, scanning the S_{Cys}–C_{Tyr} and H_{Tyr}–O_{water} coordinates. Energies are given in ΔG (kcal/mol) relative to reactants (Cu(II)–OOH + Cys-S$^•$). The lowest-energy pathway is indicated by the black arrow. (B) Spin density along the cross-link/deprotonation coordinate (broken-symmetry singlet spin surface), showing the annihilation of spin polarization as the β-spin Cys-S$^•$ radical is transferred to the Cu(II) center during the reaction, reducing it to Cu(I). Top: spin density plots (isocontour 0.004 e·Å^{-3}). Bottom: Spin density on Cu (red) and S (blue) as a function of S–C distance; points that show no spin polarization are shown in gray.

reactants, Figure 8), consistent with the barrier of the biogenesis reaction from experiment, $\Delta G^{‡} \approx 18$ kcal/mol.[17]

In this mechanistic step, the unpaired α electron of the sulfur radical attacks the aromatic ring of Tyr272, pairing with a β ring electron and causing an α electron from the ring to be transferred to the copper atom, filling the α hole of Cu(II) (Figure 9B). This forms a closed-shell singlet product (Cu(I) + Cys-Tyr$^-$ + H_2O_2), thus the reaction must occur on the singlet spin surface. As described above, H atom abstraction occurs on the triplet spin surface and affords triplet Cu(II)-OOH/Cys-S$^•$. At this point, the two spins are separated by ∼6 Å and uncoupled, enabling the cross-link to proceed on the singlet spin surface.

The final product of cofactor biogenesis forms mature Cu(I)-GO, a structure that is congruent with the known fully reduced form of the enzyme (right side of Scheme 1C) that is reactive toward O_2 during turnover.

4. DISCUSSION

4.1. One-Electron Activation of O_2 by Cu(I). The combination of Cu K-edge XAS and DFT calculations has been used to define the active-site structure of preprocessed Cu(I) galactose oxidase. The spectroscopic data reveal a three-coordinate Cu(I) center in the active site, with the metal coordinated to Tyr272, His496, and His581 residues. EXAFS data rule out sulfur coordination from the Cys228, and provide an average bond distance of the three N/O-derived ligands at 2.01 ± 0.03 Å, which is in agreement with the DFT-calculated structure of the active site (Figure 4).

The three-coordinate Cu(I) active site binds dioxygen by transferring 1e$^-$ to form a triplet end-on Cu(II)-superoxo species. The 1e$^-$ reduction of $O_{2(aq)}$ is unfavorable,[19] therefore to enable O_2 binding the enzyme must provide the driving force to compensate. O_2 binding to an open site in the mononuclear $Cu(I)_M$ site in peptidylglycine α-hydroxylating monooxygenase (PHM) is calculated to be significantly endergonic (ΔG = +18 kcal/mol);[60] therefore, in PHM, O_2 displaces a H_2O ligand to avoid an ∼10 kcal/mol penalty in $T\Delta S$ for energetically

DOI: 10.1021/jacs.6b05792
J. Am. Chem. Soc. 2016, 138, 13219−13229

accessible O_2 binding to occur. However, the Cu(I) site in GO does not have a water ligand and therefore the enzyme must overcome the unfavorable entropy of O_2 binding to an open coordination site on top of the unfavorable $1e^-$ reduction of O_2. GO thus utilizes a different strategy to activate Cu(I) for associative O_2 binding, which is by lowering the reduction potential of the Cu site through incorporation of an anionic Tyr ligand. Our computational results indicate the negative charge on the equatorial Tyr272 ligand in GO lowers the reduction potential of Cu by ~0.8 eV (compared to a neutral His ligand). This additional ~18 kcal/mol driving force imparted by the lower potential is sufficient to compensate both the entropic penalty of O_2 binding and the thermodynamic unfavorability of $1e^-$ reduction of O_2, thus enabling the cofactor biogenesis pathway (also facilitated by the coordination of the Tyr^- to the Cu, vide infra).

The ground spin state of cupric superoxides has been shown to correlate with the binding mode of $O_2^{\bullet-}$: side-on (η^2) binding results in a singlet ground state, while end-on (η^1) binding of superoxide gives a triplet ground state.[46] This has been explained in terms of a molecular orbital picture in which side-on binding results in two strong Cu−O bonds that split the two valence orbitals more than the spin-pairing energy, resulting in a singlet ground state, while the single Cu−O bonding interaction in end-on binding is weaker and cannot overcome the spin pairing energy, resulting in a triplet ground state.[46] In GO, attempts to optimize an η^2-$O_2^{\bullet-}$ structure consistently converged to the η^1-$O_2^{\bullet-}$ species in Figure 5; thus, side-on binding of $O_2^{\bullet-}$ appears to be disfavored in the active site of GO. Consistent with the generalized model,[46] end-on coordinated GO-Cu(II)-$O_2^{\bullet-}$ is calculated to have a triplet ground state (with the singlet at +6.6 kcal/mol higher in energy). The two β-LUMOs (Figure 10) show one hole

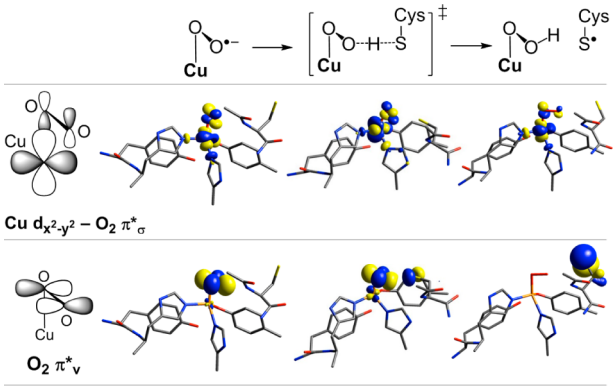

Figure 10. β-Spin LUMOs of GO-Cu(II)-$O_2^{\bullet-}$ (left), H atom abstraction transition state (center), and H atom abstraction product GO-Cu(II)-OOH + Cys-$S^\bullet$ (right). Bonding pictures of the two orbitals of GO-Cu(II)-$O_2^{\bullet-}$ are shown at left. Contours drawn at an isosurface value of ±0.05 $e{\cdot}Å^{-3}$.

localized on the superoxide in a π^* orbital oriented perpendicular to the Cu−O_2 plane (denoted π^*_v, Figure 10, bottom left) and the other hole in an orbital composed of Cu $d_{x^2-y^2}$ and O_2 π^*_σ (Figure 10, top left). Tracing these orbitals through H atom abstraction to the transition state (Figure 10, center) and product (Figure 10, right) reveals that the π^*_v orbital delocalizes onto the substrate S and is the reactive frontier molecular orbital that accepts $H^\bullet$, while the $d_{x^2-y^2} - \pi^*_\sigma$ orbital does not interact with the incoming substrate. The orientation of π^*_v also explains why the Cys-SH substrate attacks perpendicular to the Cu−O_2 plane. The π^*_v β-hole is transferred to the sulfur p orbital in the final H atom abstraction product Cys-$S^\bullet$ (Figure 10, right).

4.2. Role of Cu in Enabling Cofactor Biogenesis. In addition to enabling the $1e^-$ reduction of O_2 for H atom abstraction from Cys-SH and separating the two resulting spins to allow crossover from triplet to singlet, the Cu(II) cofactor has an essential role in facilitating the Cys-Tyr cross-link by serving as the terminal electron acceptor (Figure 11A, bottom).

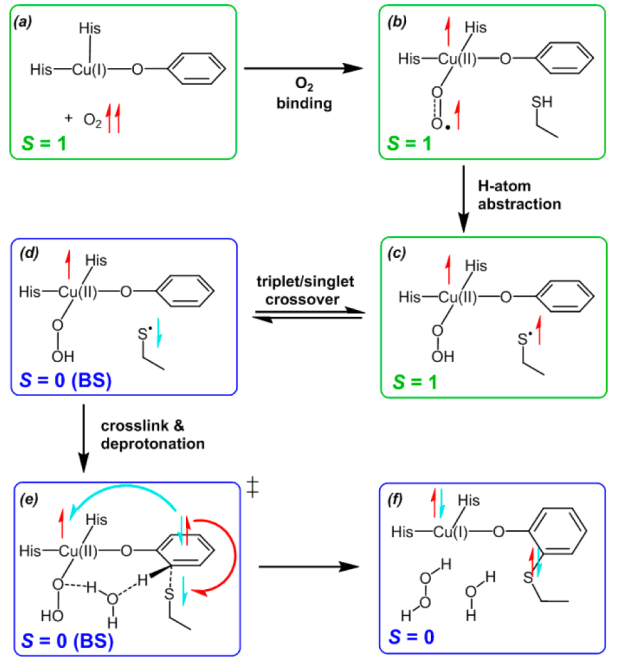

Figure 11. Summary of the cofactor biogenesis mechanism. After crossover to the singlet spin surface ($c \rightarrow d$), cross-link/deprotonation ($d \rightarrow e \rightarrow f$) is enabled by a spin pair forming from the Cys-$S^\bullet$ β electron and an α electron in a Tyr π orbital, with the remaining β Tyr electron transferred to the Cu β hole and forming closed-shell Cu(I) and $(Cys\text{-}Tyr)^-$ products (f).

During the cross-link/deprotonation, the attack of Cys-$S^\bullet$ on Tyr^- transfers an extra electron that must be accounted for. Without the availability of Cu or another electron acceptor, this electron would remain in a high energy Tyr π^* LUMO, resulting in a reaction barrier too high to allow biogenesis to proceed. Instead, an electron pair in the Tyr π HOMO provides an α electron to pair with the Cys-$S^\bullet$ β, forming the new C−S bond, and the corresponding Tyr β electron in the Tyr HOMO is transferred to the Cu(II), giving the closed-shell Cu(I) and $(Cys\text{-}Tyr)^-$ products (Figure 11f). Thus, the biogenesis mechanism is unified since each step requires Cu to (1) provide a low-potential electron to reduce O_2 by $1e^-$ and enable H atom abstraction from Cys-SH, (2) enable crossover from the triplet spin surface to the singlet, and (3) serve as the terminal electron acceptor to enable cross-link/deprotonation.

4.3. Correlation to Experimental Data. Kinetics, pH dependence, and deuterium isotope effects have been used to study the Cu(I)-dependent aerobic cofactor biogenesis in GO.[17] In particular, the overall cofactor biogenesis reaction proceeds with a maximum first-order rate constant of ~0.5 s^{-1} at high pH under saturated O_2 (giving $\Delta G^{\ddagger}_{exp} \approx 18$ kcal/mol), consistent with the calculated barrier of the rate-determining

DOI: 10.1021/jacs.6b05792
J. Am. Chem. Soc. 2016, 138, 13219−13229

cross-linking/deprotonation step in this mechanism, $\Delta G^{\ddagger}_{calc} \approx$ 20 kcal/mol. Previous kinetic data have also determined that biogenesis is pH-dependent, with three distinct regimes.[17] Biogenesis is most rapid at high pH (with maximum rate at pH > 8) and shows no solvent kinetic isotope effect (SKIE, from the reaction in H_2O versus D_2O). At mid pH (~6–8), the biogenesis rate slows with decreasing pH with an apparent pK_a of 7.3 and a small, normal SKIE of ~1.5 is observed. These two regimes have been interpreted as involving the cysteine S–H pK_a, where at high pH cross-linking occurs between Tyr and a nonprotonated cysteine (with no SKIE), and at the mid pH regime the rate-determining step involves cleavage of the solvent-exchangeable S–H.[17] The third regime at lowest pH (<6) involves oxidation of preprocessed Cu(I)-GO to preprocessed Cu(II)-GO without formation of the cross-link, likely due to protonation of Cu(II)-$O_2^{\bullet-}$ leading to the release of $HO_2^{\bullet}$.

The mechanism derived in the present study can be correlated to the three phases observed experimentally, and suggests a different source of the pK_a effect on the reactive species, namely the Tyr C–H bond that is deprotonated during cross-linking in the rate-determining step. Although aromatic C–H bonds in phenols typically have pK_a's around 40,[65] the distortion of the ring during cross-linking could sufficiently lower the C–H pK_a to be compatible with the observed pK_a of 7.3. The calculated $\Delta\Delta G$ for deprotonation from Tyr compared to deprotonation from a distorted Tyr in the geometry of the cross-link transition state gives a calculated $\Delta pK_a \approx 29$, which means the distortion and dearomatization of Tyr by Cys-S$^{\bullet}$ lowers the C–H pK_a to ~10, which would be consistent with the observed pK_a effect. DFT calculations show that the cross-link cannot form if the product remains protonated since the barrier is too large ($\Delta G^{\ddagger}$ = 32 kcal/mol), consistent with the lack of biogenesis at low pH. Therefore, a base must be present to accept the proton during biogenesis in order to lower the barrier to be kinetically accessible. In the mid-pH regime, the acceptor would be Cu(II)–OOH, which leads directly to Cu(I) and H_2O_2 products. In this internal H^+ transfer, a localized water molecule would act as a proton relay to transfer H^+ from the α-carbon of Tyr to the proximal oxygen of Cu(II)–OOH in a Grotthuss shuttle (Figure 8) and result in a small SKIE due to the cleavage of solvent O–H at the transition state. The magnitude can be estimated from the Streitwieser approximation,[66] where the lengthening of the water O–H at the saddle point of Figure 9A (1.022 Å vs 0.958 Å in the reactant complex) predicts a SKIE of 1.61,[67] consistent with the observed magnitude of ~1.5. At high pH (i.e., at higher [HO^-]), deprotonation by hydroxide would become more kinetically favorable than internal proton transfer since HO^- is a better base than Cu(II)–OOH[68] and would result in a lower barrier due to the less ordered transition state than a Grotthuss mechanism. Deprotonation by hydroxide would also have no primary SKIE since there is very little change in the O–H bond length between HO^- (0.98 Å) and H_2O (0.96 Å),[69] consistent with the experimental lack of a SKIE at high pH. In summary, reactivity in the lowest pH regime is driven by superoxide protonation (Figure 12, bottom) that supersedes biogenesis. In the middle pH regime, biogenesis proceeds by allowing internal H^+ transfer to Cu(II)–OOH during cross-link/deprotonation (Figure 12, middle), and at high pH cross-link/deprotonation occurs with H^+ transfer to HO^- without a SKIE (Figure 12, top).

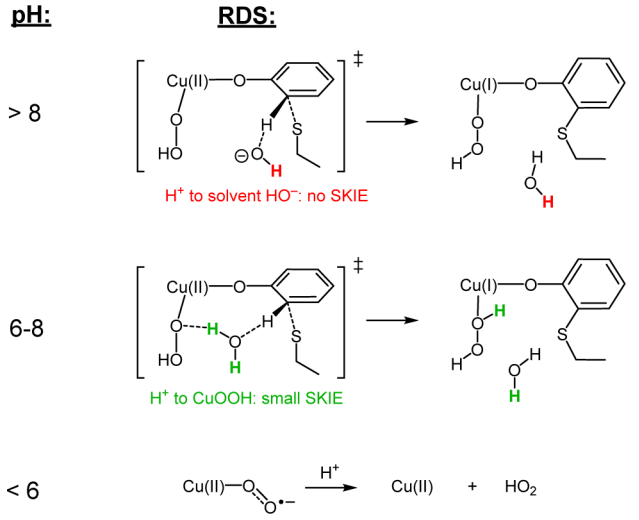

Figure 12. pH-dependent rate-determining step (RDS) and solvent kinetic isotope effect in cofactor biogenesis, with the isotope-labeled solvent hydrogens indicated. Below pH ~ 6 (bottom), superoxide protonation is faster than biogenesis. The base allowing cross-link/deprotonation at middle and high pH is Cu(II)–OOH via a Grotthuss shuttle (middle) and HO^- (top), respectively.

5. CONCLUSIONS

The active-site structure of Cu(I)-bound galactose oxidase has been determined using X-ray absorption spectroscopy (XANES and EXAFS), and density-functional theory calculations have identified a kinetically competent mechanism for cofactor biogenesis. The three-coordinate, T-shaped Cu(I) site has a low reduction potential owing to the anionic Tyr ligand, which provides sufficient driving force to overcome the thermodynamically unfavorable 1e$^-$ reduction of O_2 and coordination to an open site on Cu(I). The Cu(II)–$O_2^{\bullet-}$ intermediate is calculated to have superoxide bound in an end-on (η^1) fashion, and a triplet ground state that opens the O_2 π^*_v β-LUMO toward H atom abstraction from Cys-SH. Subsequently, Cys-Tyr cross-linking, Tyr α-carbon deprotonation, and reduction of Cu(II) to Cu(I) occur in a concerted, rate-limiting step with an overall calculated barrier of $\Delta G^{\ddagger} \approx 20$ kcal/mol. Key roles of the copper site which enable cofactor biogenesis include accessing H atom abstraction chemistry through the 1e$^-$ reduction of O_2 to $O_2^{\bullet-}$, and serving as a terminal acceptor for the extra electron during cross-linking. This study highlights the multifaceted role of copper in facilitating aerobic substrate activation, particularly how a single Cu site can be used to control 1e$^-$ O_2 reactivity in biology.

■ ASSOCIATED CONTENT

Supporting Information

The Supporting Information is available free of charge on the ACS Publications website at DOI: 10.1021/jacs.6b05792.

Additional EXAFS fits, H atom abstraction thermodynamics, and Cartesian coordinates of optimized species (PDF)

■ AUTHOR INFORMATION

Corresponding Authors

*Edward.Solomon@stanford.edu
*DaveDooley@uri.edu

DOI: 10.1021/jacs.6b05792
J. Am. Chem. Soc. 2016, 138, 13219–13229

Present Addresses

[⊥]J.C.: Departament de Química Inorgànica and Institut de Recerca de Química Teòrica i Computacional, Universitat de Barcelona, Diagonal 645, 08028 Barcelona, Spain.
[#]D.R.: Department of Chemistry, Whitman College, Walla Walla, WA 99362.

Notes

The authors declare no competing financial interest.

■ ACKNOWLEDGMENTS

We are grateful to the National Institutes of Health for research support under awards DK31450 to E.I.S.; GM27659 to D.M.D.; P41-RR001209 to K.O.H.; and Ruth L. Kirschstein National Research Service Award F32-GM105288 to R.E.C. Portions of this research were carried out at the Stanford Synchrotron Radiation Lightsource (SSRL), a Directorate of SLAC National Accelerator Laboratory and an Office of Science User Facility operated for the U.S. Department of Energy (DOE) Office of Science by Stanford University. The SSRL Structural Molecular Biology Program is supported by the DOE Office of Biological and Environmental Research and by the National Institutes of Health, National Institute of General Medical Sciences (P41-GM103393). The contents in this publication are solely the responsibility of the authors and do not necessarily represent the official view of NIGMS or NIH.

■ REFERENCES

(1) Whittaker, J. W. *Chem. Rev.* **2003**, *103*, 2347.
(2) Avigad, G.; Amaral, D.; Asensio, C.; Horecker, B. L. *J. Biol. Chem.* **1962**, *237*, 2736.
(3) Kosman, D. J.; Ettinger, M. J.; Weiner, R. E.; Massaro, E. J. *Arch. Biochem. Biophys.* **1974**, *165*, 456.
(4) Whittaker, J. W. In *Copper-Containing Proteins*; Valentine, J. S., Gralla, E. B., Eds.; Elsevier Academic Press Inc: San Diego, 2002; Vol. *60*, p 1.
(5) Parikka, K.; Master, E.; Tenkanen, M. *J. Mol. Catal. B: Enzym.* **2015**, *120*, 47.
(6) Matsumura, S.; Kuroda, A.; Higaki, N.; Hiruta, Y.; Yoshikawa, S. *Chem. Lett.* **1988**, *17*, 1747.
(7) Kelleher, F. M.; Bhavanandan, V. P. *J. Biol. Chem.* **1986**, *261*, 11045.
(8) Some recently identified members of the alcohol oxidase family are essentially inactive towards galactose but efficiently catalyze oxidation of other aliphatic alcohols. See: Yin, D.; Urresti, S.; Lafond, M.; Johnston, E. M.; Derikvand, F.; Ciano, L.; Berrin, J.-G.; Henrissat, B.; Walton, P. H.; Davies, G. J.; Brumer, H. *Nat. Commun.* **2015**, *6*, 10197.
(9) An enzyme similar to GO posessing a Cu/(Cys-Tyr) cofactor has been recently described in actinobacteria, where it is implicated in glycan synthesis during bacterial morphogenesis. See: Chaplin, A. K.; Petrus, M. L. C.; Mangiameli, G.; Hough, M. A.; Svistunenko, D. A.; Nicholls, P.; Claessen, D.; Vijgenboom, E.; Worrall, J. A. R. *Biochem. J.* **2015**, *469*, 433.
(10) Kanyong, P.; Pemberton, R. M.; Jackson, S. K.; Hart, J. P. *Anal. Biochem.* **2013**, *435*, 114.
(11) Sharma, S. K.; Singhal, R.; Malhotra, B. D.; Sehgal, N.; Kumar, A. *Electrochim. Acta* **2004**, *49*, 2479.
(12) Dalkıran, B.; Erden, P. E.; Kılıç, E. *Anal. Bioanal. Chem.* **2016**, *408*, 4329.
(13) Rokhsana, D.; Howells, A. E.; Dooley, D. M.; Szilagyi, R. K. *Inorg. Chem.* **2012**, *51*, 3513.
(14) Ito, N.; Phillips, S. E. V.; Stevens, C.; Ogel, Z. B.; McPherson, M. J.; Keen, J. N.; Yadav, K. D. S.; Knowles, P. F. *Nature* **1991**, *350*, 87.
(15) Rogers, M. S.; Tyler, E. M.; Akyumani, N.; Kurtis, C. R.; Spooner, R. K.; Deacon, S. E.; Tamber, S.; Firbank, S. J.; Mahmoud, K.; Knowles, P. F.; Phillips, S. E. V.; McPherson, M. J.; Dooley, D. M. *Biochemistry* **2007**, *46*, 4606.
(16) Firbank, S. J.; Rogers, M. S.; Wilmot, C. M.; Dooley, D. M.; Halcrow, M. A.; Knowles, P. F.; McPherson, M. J.; Phillips, S. E. V. *Proc. Natl. Acad. Sci. U. S. A.* **2001**, *98*, 12932.
(17) Whittaker, M. M.; Whittaker, J. W. *J. Biol. Chem.* **2003**, *278*, 22090.
(18) Rogers, M. S.; Hurtado-Guerrero, R.; Firbank, S. J.; Halcrow, M. A.; Dooley, D. M.; Phillips, S. E. V.; Knowles, P. F.; McPherson, M. J. *Biochemistry* **2008**, *47*, 10428.
(19) Wood, P. M. *Biochem. J.* **1988**, *253*, 287.
(20) Humphrey, W.; Dalke, A.; Schulten, K. *J. Mol. Graphics* **1996**, *14*, 33.
(21) Tenderholt, A.; Hedman, B.; Hodgson, K. O. *AIP Conf. Proc.* **2006**, *882*, 105.
(22) George, G. N. *EXAFSPAK*, Stanford Synchrotron Radiation Laboratory: Menolo Park, CA, 2000.
(23) Rehr, J. J.; Albers, R. C. *Rev. Mod. Phys.* **2000**, *72*, 621.
(24) Frisch, M. J.; Trucks, G. W.; Schlegel, H. B.; Scuseria, G. E.; Robb, M. A.; Cheeseman, J. R.; Scalmani, G.; Barone, V.; Mennucci, B.; Petersson, G. A.; Nakatsuji, H.; Caricato, M.; Li, X.; Hratchian, H. P.; Izmaylov, A. F.; Bloino, J.; Zheng, G.; Sonnenberg, J. L.; Hada, M.; Ehara, M.; Toyota, K.; Fukuda, R.; Hasegawa, J.; Ishida, M.; Nakajima, T.; Honda, Y.; Kitao, O.; Nakai, H.; Vreven, T.; Montgomery, J. A., Jr.; Peralta, J. E.; Ogliaro, F.; Bearpark, M. J.; Heyd, J.; Brothers, E. N.; Kudin, K. N.; Staroverov, V. N.; Kobayashi, R.; Normand, J.; Raghavachari, K.; Rendell, A. P.; Burant, J. C.; Iyengar, S. S.; Tomasi, J.; Cossi, M.; Rega, N.; Millam, N. J.; Klene, M.; Knox, J. E.; Cross, J. B.; Bakken, V.; Adamo, C.; Jaramillo, J.; Gomperts, R.; Stratmann, R. E.; Yazyev, O.; Austin, A. J.; Cammi, R.; Pomelli, C.; Ochterski, J. W.; Martin, R. L.; Morokuma, K.; Zakrzewski, V. G.; Voth, G. A.; Salvador, P.; Dannenberg, J. J.; Dapprich, S.; Daniels, A. D.; Farkas, Ö.; Foresman, J. B.; Ortiz, J. V.; Cioslowski, J.; Fox, D. J. *Gaussian 09*, Gaussian, Inc.: Wallingford, CT, 2009.
(25) Szilagyi, R. K.; Metz, M.; Solomon, E. I. *J. Phys. Chem. A* **2002**, *106*, 2994.
(26) Kau, L. S.; Spira-Solomon, D. J.; Penner-Hahn, J. E.; Hodgson, K. O.; Solomon, E. I. *J. Am. Chem. Soc.* **1987**, *109*, 6433.
(27) Hendriks, H. M. J.; Birker, J. M. W. L.; Van Rijn, J.; Verschoor, G. C.; Reedijk, J. *J. Am. Chem. Soc.* **1982**, *104*, 3607.
(28) Sorrell, T. N.; Malachowski, M. R.; Jameson, D. L. *Inorg. Chem.* **1982**, *21*, 3250.
(29) Karlin, K. D.; Hayes, J. C.; Hutchinson, J. P.; Hyde, J. R.; Zubieta, J. *Inorg. Chim. Acta* **1982**, *64*, L219.
(30) 2- and 4-Coordinate fits were also attempted. A 2-coordinate model significantly underfit the large intensity of the first shell (see Figure S5). A 4-coordinate fit could be accommodated, but did not improve the fit compared to 3-coordinate. Therefore, the EXAFS are best fit with a 3-coordinate first shell, consistent with the XANES.
(31) Brown, I. D.; Altermatt, D. *Acta Crystallogr., Sect. B: Struct. Sci.* **1985**, *B41*, 244.
(32) Thorp, H. H. *Inorg. Chem.* **1992**, *31*, 1585.
(33) Brown, I. D. *The Chemical Bond in Inorganic Chemistry: The Bond Valence Model*; Oxford University Press: Oxford, 2002.
(34) Osborne, J. P.; Cosper, N. J.; Stålhandske, C. M. V.; Scott, R. A.; Alben, J. O.; Gennis, R. B. *Biochemistry* **1999**, *38*, 4526.
(35) Dooley, D. M.; Scott, R. A.; Knowles, P. F.; Colangelo, C. M.; McGuirl, M. A.; Brown, D. E. *J. Am. Chem. Soc.* **1998**, *120*, 2599.
(36) Shearer, J.; Szalai, V. A. *J. Am. Chem. Soc.* **2008**, *130*, 17826.
(37) Arcos-López, T.; Qayyum, M.; Rivillas-Acevedo, L.; Miotto, M. C.; Grande-Aztatzi, R.; Fernández, C. O.; Hedman, B.; Hodgson, K. O.; Vela, A.; Solomon, E. I.; Quintanar, L. *Inorg. Chem.* **2016**, *55*, 2909.
(38) $r_0 = r_c + Ar_a + P - D - F$ is eq 5 from ref 31, where r_c is the crystallographic radius of the cation (1.895 Å for Cu), A is an empirical parameter (0.8 for transition metal centers), r_a is the contribution from the crystallographic radius of the anion (0.09 Å for N and 0.00 Å for O), and P, D, and F are corrections for the number of p, d, and f electrons on the cation (P = 0.035 and F = 0 for Cu, and D = 0.38 for d^{10} systems).

DOI: 10.1021/jacs.6b05792
J. Am. Chem. Soc. 2016, 138, 13219−13229

(39) From a survey of 201 crystal structures in the Cambridge Structural Database published since 2006 of three-coordinate Cu(I) complexes containing only N or O ligands, the average Cu−N/O bond length in three-coordinate Cu(I) complexes is 1.979 ± 0.09 Å. CSD ver. 5.37 (May 2016 update): Groom, C. R.; Bruno, I. J.; Lightfoot, M. P.; Ward, S. C. *Acta Crystallogr., Sect. B: Struct. Sci., Cryst. Eng. Mater.* **2016**, *B72*, 171−179.
(40) These include a 2-coordinate structure with His581/Tyr495 (+5.1 kcal/mol) and 3-coordinate structures with His581/Tyr495/Tyr272 and either Tyr272 deprotonated (+14.8 kcal/mol) or both Tyr272 and Tyr495 deprotonated (+46.3 kcal/mol). No structure was stable with both His496 and Tyr495 coordinated; the parallel orientation of these residues imposed by the backbone prevents both from simultaneously coordinating to Cu.
(41) Chen, P.; Root, D. E.; Campochiaro, C.; Fujisawa, K.; Solomon, E. I. *J. Am. Chem. Soc.* **2003**, *125*, 466.
(42) Aboelella, N. W.; Kryatov, S. V.; Gherman, B. F.; Brennessel, W. W.; Young, V. G., Jr.; Sarangi, R.; Rybak-Akimova, E. V.; Hodgson, K. O.; Hedman, B.; Solomon, E. I.; Cramer, C. J.; Tolman, W. B. *J. Am. Chem. Soc.* **2004**, *126*, 16896.
(43) Fujisawa, K.; Tanaka, M.; Moro-oka, Y.; Kitajima, N. *J. Am. Chem. Soc.* **1994**, *116*, 12079.
(44) Sanchez-Eguia, B. N.; Flores-Alamo, M.; Orio, M.; Castillo, I. *Chem. Commun.* **2015**, *51*, 11134.
(45) Woertink, J. S.; Tian, L.; Maiti, D.; Lucas, H. R.; Himes, R. A.; Karlin, K. D.; Neese, F.; Würtele, C.; Holthausen, M. C.; Bill, E.; Sundermeyer, J.; Schindler, S.; Solomon, E. I. *Inorg. Chem.* **2010**, *49*, 9450.
(46) Ginsbach, J. W.; Peterson, R. L.; Cowley, R. E.; Karlin, K. D.; Solomon, E. I. *Inorg. Chem.* **2013**, *52*, 12872.
(47) Peterson, R. L.; Ginsbach, J. W.; Cowley, R. E.; Qayyum, M. F.; Himes, R. A.; Siegler, M. A.; Moore, C. D.; Hedman, B.; Hodgson, K. O.; Fukuzumi, S.; Solomon, E. I.; Karlin, K. D. *J. Am. Chem. Soc.* **2013**, *135*, 16454.
(48) Kim, S.; Lee, J. Y.; Cowley, R. E.; Ginsbach, J. W.; Siegler, M. A.; Solomon, E. I.; Karlin, K. D. *J. Am. Chem. Soc.* **2015**, *137*, 2796.
(49) Würtele, C.; Gaoutchenova, E.; Harms, K.; Holthausen, M. C.; Sundermeyer, J.; Schindler, S. *Angew. Chem., Int. Ed.* **2006**, *45*, 3867.
(50) Maiti, D.; Fry, H. C.; Woertink, J. S.; Vance, M. A.; Solomon, E. I.; Karlin, K. D. *J. Am. Chem. Soc.* **2007**, *129*, 264.
(51) Peterson, R. L.; Himes, R. A.; Kotani, H.; Suenobu, T.; Tian, L.; Siegler, M. A.; Solomon, E. I.; Fukuzumi, S.; Karlin, K. D. *J. Am. Chem. Soc.* **2011**, *133*, 1702.
(52) Jazdzewski, B.; Reynolds, A.; Holland, P.; Young, V., Jr.; Kaderli, S.; Zuberbühler, A.; Tolman, W. *J. Biol. Inorg. Chem.* **2003**, *8*, 381.
(53) Kunishita, A.; Ertem, M. Z.; Okubo, Y.; Tano, T.; Sugimoto, H.; Ohkubo, K.; Fujieda, N.; Fukuzumi, S.; Cramer, C. J.; Itoh, S. *Inorg. Chem.* **2012**, *51*, 9465.
(54) Kunishita, A.; Kubo, M.; Sugimoto, H.; Ogura, T.; Sato, K.; Takui, T.; Itoh, S. *J. Am. Chem. Soc.* **2009**, *131*, 2788.
(55) Kobayashi, Y.; Ohkubo, K.; Nomura, T.; Kubo, M.; Fujieda, N.; Sugimoto, H.; Fukuzumi, S.; Goto, K.; Ogura, T.; Itoh, S. *Eur. J. Inorg. Chem.* **2012**, *2012*, 4574.
(56) Tano, T.; Okubo, Y.; Kunishita, A.; Kubo, M.; Sugimoto, H.; Fujieda, N.; Ogura, T.; Itoh, S. *Inorg. Chem.* **2013**, *52*, 10431.
(57) Itoh, S. *Acc. Chem. Res.* **2015**, *48*, 2066.
(58) Donoghue, P. J.; Gupta, A. K.; Boyce, D. W.; Cramer, C. J.; Tolman, W. B. *J. Am. Chem. Soc.* **2010**, *132*, 15869.
(59) Lee, J. Y.; Peterson, R. L.; Ohkubo, K.; Garcia-Bosch, I.; Himes, R. A.; Woertink, J.; Moore, C. D.; Solomon, E. I.; Fukuzumi, S.; Karlin, K. D. *J. Am. Chem. Soc.* **2014**, *136*, 9925.
(60) Chen, P.; Solomon, E. I. *J. Am. Chem. Soc.* **2004**, *126*, 4991.
(61) Chen, P.; Solomon, E. I. *Proc. Natl. Acad. Sci. U. S. A.* **2004**, *101*, 13105.
(62) Agmon, N. *Chem. Phys. Lett.* **1995**, *244*, 456.
(63) Grotthuss, C. J. T. *Ann. Chim.* **1806**, *58*, 54.
(64) The position of the Cys prevents direct deprotonation by the proximal O of the hydroperoxide, and therefore, the water bridge is required to transfer the proton without steric crowding.
(65) Fraser, R. R.; Bresse, M.; Mansour, T. S. *J. Am. Chem. Soc.* **1983**, *105*, 7790.
(66) Streitwieser, A.; Jagow, R. H.; Fahey, R. C.; Suzuki, S. *J. Am. Chem. Soc.* **1958**, *80*, 2326.
(67) For the Streitwieser approximation,

$$\frac{k_D}{k_H} = \exp\left\{-\frac{hc}{2kT}\left[\sum(\nu_D^{\ddagger} - \nu_H^{\ddagger}) - \sum(\nu_D - \nu_H)\right]\right\}$$

ν_H and ν_D are the normal-mode frequencies for H and D isotopologues of the reactant and $\nu_H^{\ddagger}$ and $\nu_D^{\ddagger}$ are the corresponding frequencies for H and D isotopologues at the transition state. For the Streitwieser calculation, normal-mode frequencies were calculated for a H_2O molecule frozen at the geometry of the localized water at the reaction saddle point, and compared to those for H_2O frozen at the geometry of the reactant complex. All three normal modes were included in the calculation.
(68) The pK_a of H_2O_2 coordinated to tetrakis(imidazole)copper(II) is 8.6; see: Ferreira, A. M. C.; Toma, H. E. *J. Coord. Chem.* **1988**, *18*, 351.
(69) *Tables of Interatomic Distances and Configuration in Molecules and Ions*; Sutton, L. E., Ed.; The Chemical Society: London, 1965.

DOI: 10.1021/jacs.6b05792
J. Am. Chem. Soc. 2016, 138, 13219−13229